Monthly Notices of the ROYAL ASTRONOMICAL SOCIETY

MNRAS **532,** 965–981 (2024)
Advance Access publication 2024 June 20

https://doi.org/10.1093/mnras/stae1528

Automated detection and analysis of coronal active region structures across solar cycle 24

Daniel G. Gass ★ and Robert W. Walsh★

Jeremiah Horrocks Institute, School of Engineering and Computing, University of Central Lancashire, Fylde Rd, Lancashire, Preston PR1 2HE, UK

Accepted 2024 June 18. Received 2024 June 14; in original form 2023 May 17

ABSTRACT

Observations from NASA's Solar Dynamic Observatory Atmospheric Imaging Assembly were employed to investigate targeted physical properties of coronal active region structures across the majority of solar cycle 24 (From 2010 May to end of 2020 December). This is the largest consistent study to date which analyses emergent trends in structural width, location, and occurrence rate by performing an automatic and long-term examination of observable coronal and chromospheric limb features within equatorial active region belts across four extreme ultraviolet wavelengths (171, 193, 211, and 304 Å). This has resulted in over 30 000 observed coronal structures and hence allows for the production of spatial and temporal distributions focused upon the rise, peak, and decay activity phases of solar cycle 24. Employing a self-organized-criticality approach as a descriptor of coronal structure formation, power-law slopes of structural widths versus frequency are determined, ranging from -1.6 to -3.3 with variations of up to 0.7 found between differing periods of the solar cycle, compared to a predicted Fractal Diffusive Self-Organized Criticality (FD-SOC) value of -1.5. The North–South hemispheric asymmetry of these structures was also examined with the Northern hemisphere exhibiting activity that is peaking earlier and decaying slower than the Southern hemisphere, with a characteristic 'butterfly' pattern of coronal structures detected. This represents the first survey of coronal structures performed across an entire solar cycle, demonstrating new techniques available to examine the composition of the corona by latitude in varying wavelengths.

Key words: Sun: atmosphere – Sun: corona – Sun: UV radiation.

1 INTRODUCTION

1.1 The solar cycle and active regions

The 11 yr solar activity cycle, as part of the larger 22 yr solar magnetic cycle, is one of the clearest observable indicators of the Sun's complex and dynamic magnetic field. This change in activity and polarity has clear consequences for the wider heliosphere and space weather in the form of solar flares, coronal mass ejections (CMEs), and UV irradiance. However, the specifics of how this varying magnetic activity can propagate outwardly into the corona and further within the heliosphere is still not fully understood.

Coronal structures such as loops and plumes are observable consequences of the sun's magnetic field (Reale 2014). Though these structures have been extensively imaged over solar cycle 24 by instruments such as NASA's Solar Dynamics Observatory (SDO) Atmospheric Imaging Assembly (AIA) (Lemen et al. 2012; Pesnell, Thompson & Chamberlin 2012), these rich and expansive data sets have not always been fully leveraged to take advantage of this long-term coverage. Previous studies have focused on the aspects of specific properties of coronal structures such as the cross-sectional profiles and morphology (Klimchuk & DeForest 2020), lengths (Dahlburg et al. 2018), intensities and temperatures (Xie et al. 2017), and the interaction of complex magnetic regions (Rappazzo 2015). These approaches are typically limited in scope, utilizing targeted portions of the data available, focusing on a few active regions and relatively short time periods. The evolution of these properties and any possible connection across the solar cycle therefore is not fully appreciated.

Active regions are areas of predominantly closed magnetic flux occurring roughly 30 deg above and below the line of the solar equator (van Driel-Gesztelyi & Green 2015) at the start of the solar cycle and migrating towards the line of the equator as the cycle progresses. These are referred to as the active region belts and are indicators of the phases of magnetic activity across the solar cycle (Hathaway 2015). The solar magnetic field can vary in strength drastically by region and latitude and is also associated with a high degree of dynamism and magnetic field intensity variation (Kuckein et al. 2009; Brooks, Warren & Landi 2021), with high temperature and velocity variations across plasma structures. This makes it a particularly compelling region for research into the interactions of plasma with these strong, varying magnetic fields (Higginson et al. 2017; Seaton et al. 2021).

These regions of magnetic activity can exhibit highly complex braiding behaviours between and within magnetic flux tubes on a wide variety of spatial scales (Chitta et al. 2022). A combination

★ E-mail: danielgass192@gmail.com (DGG); RWWalsh@uclan.ac.uk (RWW)

of motions from photospheric driving waves (AC heating, Milano, Gómez & Martens 1997) causes local reconnections and realignments of the magnetic field and dissipation between current sheets (DC nanoflare heating, Moriyasu et al. 2004) and Joule heating (Kanella & Gudiksen 2019); both likely contribute to the heating of coronal plasma. As heated plasma fills the flux tubes which constrains them, this plasma radiates at specific wavelengths, and coronal structures are observed. Thus, the placement and observed width of these structures should be informative of the physical processes and the magnetic conditions which produced them. Coronal plasma structures can be broadly categorized as loops or plumes by their magnetic openness. Structures which are magnetically closed within the local solar atmosphere are commonly known as loops, which will be the primary objective for this study, and will be referred to as such throughout this paper. Structures which are magnetically open are referred to as plumes, and occur more frequently away from the closed active regions.

The aim of this work then is to identify and record the largest possible population of coronal structures across solar cycle 24 by measuring and studying the evolution of coronal loop width, latitude, and occurrence frequency. This will allow for novel analysis of the corona – measuring specific changes to many of these parameters and contrasting them to other well-known indicators of solar activity such as sunspots, models of predictions of coronal loop parameter distribution, and against the properties of other loops recorded in multiple EUV wavelengths.

1.2 Coronal structures and observation

Coronal structures are pervasive fundamental features of the solar corona (Reale 2014). These structures vary greatly in length, from a few hundred kilometres in very small loops to several solar radii for extended plumes. There are a variety of models utilizing a wide range of magnetohydrodynamical (MHD) based heating scenarios (see reviews such as Heyvaerts & Priest 1984 and Milano et al. 1997).

Limitations of coronal observations are imposed both by instrumental effects and viewing conditions of the corona. Some limitations, such as strong and complex background noise can be mitigated by choosing structures present at the coronal limb, but others, such as the point spread function and charge spreading effects, are non-trivial to deconvolve from images (Poduval et al. 2013) and can effectively destroy information from smaller structures.

A summary on existing coronal loop observations made with various instruments is provided by Aschwanden & Peter (2017); they outline the decreasing minimum observable loop width that is brought about as a consequence of improving instrumental resolving power. They describe loop width as a combination of the true width size and any possible perceived loop broadening which are observational effects, described as the following:

$$w_{\rm obs}^2 = w_{\rm psf}^2 + w_{\rm true}^2 + w_{\rm noise}^2, \quad (1)$$

where $w_{\rm obs}$ is the observed loop width, $w_{\rm true}$ is the 'true' loop width, or how large the structure would appear if viewed without any limiting effects; $w_{\rm psf}$ is the point spread function introduced by the instrument effects such as diffraction patterns introduced by filters (in the case of AIA), charge spreading in the CCD, etc; and finally, $w_{\rm noise}$ is the broadening caused by noise effects such as Poissonian photon noise, dark current, readout noise. For EUV AIA wavelengths, this minimum observed size $w_{\rm obs}$ is approximately 2.7 pixels.

1.3 Coronal widths and self-organized criticality

Self-Organized Criticality (SOC) (Bak, Tang & Wiesenfeld 1987, 1988) is a statistical model used to approximate the behaviour of various physical systems composed of numerous elements, such as grains being added to a pile of sand in the original Bak et al. (1987) study. These elements have local critical thresholds, and one of the defining features of SOC systems is their ability to naturally evolve towards a globally critical state. In this state, the system exhibits complex behaviours, often characterized by larger avalanching events resulting from small-scale interactions among its components.

In a globally critical state, SOC systems are highly sensitive to even small perturbations. This means that the addition of energy or disturbances at any point within the system can trigger system-wide behaviours and large-scale cascades of events. These cascades follow a particular statistical pattern known as a power-law distribution, denoted here as D(S). In the context of SOC, this distribution is scale-invariant, which means that the behaviour appears consistently across various orders of magnitude.

The requirements for a system to be approximated by an SOC model are as follows: (i) there are a large number of interacting components or elements within the system, and that these elements interact in a non-linear manner, (ii) that the system has some critical threshold after which it becomes extremely sensitive to small-scale perturbations, (iii) the system evolves to this threshold over time without interference, and (iv) that the behaviour of these perturbations is consistent across many scales, and exhibit characteristic power-law distributions.

Across the solar atmosphere, the interaction of magnetic flux elements which undergo reconnection to form the appearance of coronal structures (the DC heating scenario) are potentially consistent with the description above. This includes (i) that the requirements of stochastic addition (energy deposited randomly within subresolved structures), (ii) the existence of a local critical threshold (the amount of energy which is needed to trigger the process of magnetic process), (iii) the multiscale nature of the space (subresolved flux tubes of scale lengths potentially stretching from tens of km up to tens of thousands of km), and (iv) the presence of a global critical state by which small-scale events can spread and cascade into larger events which themselves spread throughout the space (local magnetic reconnection activity perturbs adjacent filaments which cause further reconnection events to occur). Taken as a whole, this implies that some characteristic statistics of SOC processes might be detectable within large enough samples of these coronal structures.

Thus, if during the investigation of certain physical properties of coronal features a power law is observed that is similar to those predicted by SOC, then the degree to which the DC heating scenario is applicable could be determined. This power law could potentially be observable in different parameters such as coronal widths, which are an analogue to the D(S), assuming that observably wider structures are indicative of a greater number of reconnection events that take place.

A strength of the SOC approach is that it does not rely on a precise understanding of the exact mechanisms which are operating within the observed region. Therefore, highly complex 3D MHD reconnection simulations are not required for approximating local conditions within the corona. Rather, with SOC, the local requirement of exceeding some critical threshold in some parameter(s) alleviates the requirement for the entire system to be solved for predictions of observational parameters. SOC has already been shown to apply to a number of physical and astrophysical phenomenon (Watkins et al. 2016), including in reconnection in solar flares, CMEs, and

solar energetic particles (Sharma et al. 2016). Although SOC-based analysis will allow for a greater degree of physical interpretation of coronal loop populations and their connection to the magnetic changes which occur in the solar cycle in bulk, there are some caveats. It must be noted that the aforementioned observational limitations will introduce a threshold cut-off effect to the power law of observed coronal structural widths. This effect thresholds the distribution of observed SOC events viewed by AIA, including coronal structures below the 2.7 pixel limit described above. These observational effects combined with any possible variation to underlying physical and magnetic processes driven by the solar cycle could cause a measurable deviation from a predicted SOC gradient. Thus by examining any deviation from ideal values derived from stochastic, fractal events in n-dimensional SOC space (-1.5 in the case of coronal loop widths, which are taken to be analogues for the size s of cascading events), systemic differences that arise from non-observable effects can be quantified .

The power law predicted by the ideal Fractal Diffusive (FD) SOC is indicative of the presence of coupled, driven oscillators and the dissipative non-linear avalanching behaviour, which spreads across all available scale lengths given a stochastic driver. As this model is not informed by physical processes and does not include effects which are non-avalanching, it can be assumed that the simple SOC approach is not wholly descriptive of the physical phenomenon occurring in the environment of the solar corona during loop formation; deviations from this ideal value can be described as combinations of observational effects, and contributions from physical processes unrelated to those which are approximated by SOC. These variations can also be described by modification of the simple ideal case.

Prior results from studies of active regions demonstrate SOC distributions within coronal loop population widths, finding power-law slopes for structures ranging from roughly -2.7 to -3.3 for active regions viewed in multiple AIA filters and around -1.39 in loops as viewed by the Hi-C instrument (Aschwanden & Peter 2017; Zhiming et al. 2019). This compares to an 'ideal' FD-SOC gradient of -1.5, indicating that higher resolution images of coronal structures yield results more aligned with those predicted by SOC.

The difference between observed coefficients of power-law slope of widths α_w across the solar cycle to the ideal coefficient of the power-law slope of the number of cascading events occurring as predicted by SOC α_s can be quantified and analysed. The closeness of fit between observed profiles and modelled power laws can be used to analyse loop widths. Comparing their populations from various points across the entire recent solar cycle provides a basis for the analysis of coronal structure populations in time periods and wavelengths. SOC then becomes a type of statistical probe of emergent behaviours in the corona.

1.4 North–South hemispheric asymmetry

Additionally, a long-term approach to examining coronal structures can examine North versus South hemispheric asymmetry. Imbalance in northern and southern solar magnetic activity has been observed for several decades (Bell & Glazer 1958) and has been explored extensively in a variety of solar phenomenon such as sunspot activity (Javaraiah 2021), interplanetary energetic and geomagnetic indicators (El-Borie et al. 2012), and sunspot rotation rates (Xie, Shi & Qu 2018). However, no large-scale study of asymmetry within coronal structures has been undertaken. Though expected to be strongly related to sunspots by their shared emerging magnetic flux tubes, it has been challenging for models to definitively determine the relationship between simple emerging flux tubes present at the footpoints of coronal structures and more developed observable structures higher in the solar atmosphere. This is due in part to the changing ratio of plasma pressure to magnetic pressure (plasma beta) with height and mechanical warping/tension of these structures. By examining this asymmetry in the context of the different EUV channels, more details of plasma temperatures and their changing distributions across the solar cycle can be obtained.

In addition to the coronal widths, the hemispheric asymmetry of structures can indicate the behaviour of the corona and its reaction to the changing activities within the asymmetric solar dynamo as they change throughout the solar cycle. Such an examination may prove useful for determining the degree of similarity between the placement coronal structures and their corresponding photospheric footpoints, such as active region sunspots, as well as in identifying divergences from these expected positions in different temperature regimes.

In the following sections, the methodology of an automated approach to the identification and measurement of coronal loops in AIA EUV images is outlined, and the techniques of analysis performed upon them described.

2 METHOD

To analyse the properties of structures of interest within the corona, they must first be identified and traced; in the case of coronal loop structures, this can be challenging for two main reasons. First, the contribution of background/foreground emission along the integrated line of sight can be significantly greater than the emission of coronal loop structures, and attempts to properly isolate loop intensity from background measurements can be challenging (Reale 2014). Secondly, there is the issue of the relative angle of the observed structure to the observer. This is not always feasible to perform in all portions of the corona in an automatic fashion, as there are a number of assumptions which must be made about the underlying loop orientation and background. This involves complex magnetic and structural topologies that visually overlap along the line of sight (Beveridge, Priest & Brown 2004), which can introduce errors to subsequent measurement (Mikić et al. 2013), especially in wavelengths in which the corona is optically thin.

To mitigate the above issues, coronal loops just above the limb were chosen as the basis of study for measurement and analysis. Limb loops are by definition observed away from the bright solar disc, thus simplifying as far as possible the contaminating background and foreground emission.

2.1 Defining time periods across the solar cycle

Solar cycle 24 is considered to have occurred from roughly 2009 to 2020 (Hathaway 2015), though by some estimates (such as by monitoring solar acoustic modes), the first detectable increases in solar activity may have occurred as early as towards the end of 2007 (Salabert et al. 2009). In this work, to attempt examining the various phases of a solar cycle, its duration was broken down into three main time periods as outlined in Fig. 1 and in more detail below:

(i) The **'Rise'** phase is defined as the time of rising solar activity, starting from a minimal base level and extending to the time when the first peak of solar sunspot activity for Cycle 24 is recorded. The Rise period is relatively short, beginning 2010 May 13 (the earliest

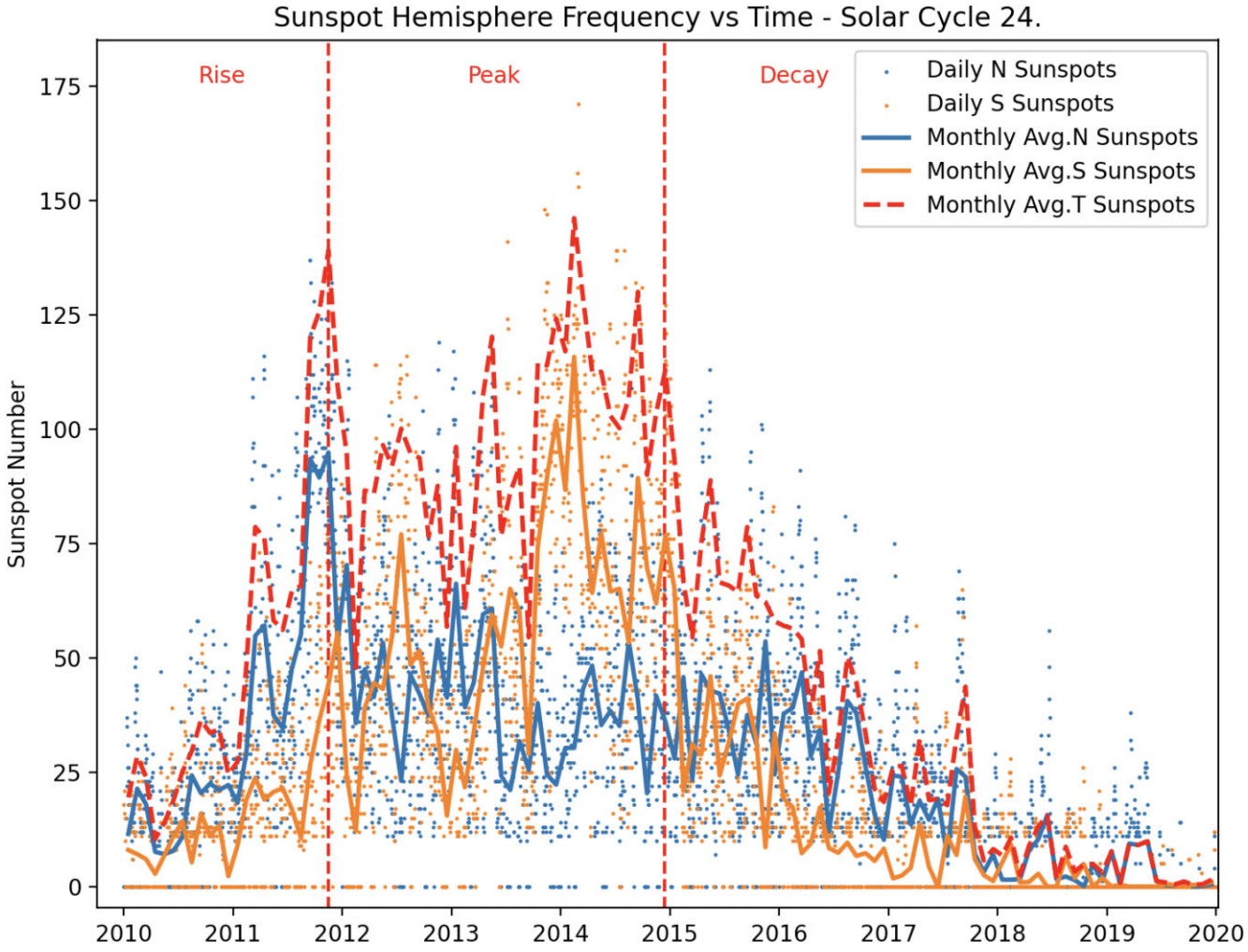

Figure 1. Sunspot hemispheric activity (y-axis) versus time (x-axis). Blue indicates northern activity, and orange indicates southern activity. The red dashed line indicates overall average sunspot number. The dots and lines indicate count by day and monthly average, respectively. Data for hemispheric occurrence of sunspots are obtained from the Sunspot Index and Long-term Solar Observations (SILSO) catalogue hosted by the Royal Observatory of Belgium (SILSO World Data Center 2020).

captured data within the AIA data base) and extending to the end of 2011 November 15.

(ii) The **'Peak'** phase is defined as the period of sustained high levels of solar activity from 2011 November 15, where sunspot count is slowly but consistently increasing or constant, until 2014 November 13, after which activity begins to decline consistently. This period contains the solar maximum for cycle 24, and corresponds to the highest quantity of observed sunspots within the cycle.

(iii) Finally, the **'Decay'** phase is defined to be the extended period of decline in solar activity, from 2014 November 15 and reaching out to the end of 2019. This is the longest phase of solar activity by time, but contains a number of years of comparatively low solar activity.

Given that AIA coverage only begins in 2010 August, it is possible that some activity at the start of Cycle 24 is not accounted for, and this would be reflected in lower numbers of structures detected in the Rise phase. However, the solar cycle is characterized by initial periods of very low activity, and this period is unlikely to have significantly influenced the characteristic distributions of coronal widths which are demonstrated in Section 3.

In subsequent sections, the solar cycle will be discussed by reference to the three phases mentioned above, and coronal structure populations analysed within each time period.

2.2 North–South hemispheric asymmetry

The North–South Hemispheric Asymmetry is a phenomenon by which observable measures of solar activity vary between Northern and Southern hemispheres depending on the polarity of the solar cycle. Quantitative measurement of this imbalance has been helped by the creation of N-S activity indexes (Carbonell, Oliver & Ballester 1993; Oliver & Ballester 1994) given as

$$AS = \frac{N - S}{N + S} \tag{2}$$

Here, the activity index AS is defined as the quotient of the difference between activity in the Northern hemisphere N, activity in the Southern hemisphere S, and the total amount of activity in both hemispheres. Though this was originally applied in the context of sunspot activity, further examinations of N-S asymmetry have been performed for other indices such as solar wind speed (Nair & Nayar 2008), solar flares (Joshi et al. 2015), and atmospheric solar plasma

density (El-Borie et al. 2017). Of these, the sunspot activity index is the most well known and documented indicator of solar magnetic activity, and will be used here as a basis of comparison to coronal structure activity.

Measuring and analysing N-S coronal asymmetry indexes as they change throughout time and as they vary from wavelength to wavelength will be beneficial for creating a more nuanced understanding of North–South asymmetry in coronal magnetic fields themselves.

2.3 Image enhancement and multi-Gaussian normalization processing

The AIA instrument contains multiple filters in the EUV regime, sensitive to plasma within the solar atmosphere above the photosphere (excluding 1600, 1700, and 4500 Å). Filters of particular interest to this study are 171, 193, 211, and 304 Å as they possess relatively narrow wavelength response functions and singly peaking temperature response functions (to within two orders of magnitude of peak response) (O'Dwyer et al. 2010). Other factors for choosing or discarding particular filters include the number of observable structures (lower in the case of very high temperature wavelengths such as 355, 94, and 131 Å), the degradation of CCDs, and the predominance of diffuse structures which are difficult to detect.

In spite of degradation apparent across Solar Cycle 24, 304 Å is included in particular due to its relevance for comparison to contemporary instruments (such as Solar Orbiter which possesses 171 and 304 Å filters), and also because its observation of chromospheric structures is unique within the AIA instrument. This experiment will also attempt to determine if enough 304 Å structures are visible in the imaged regions to analyse their properties, extending the impact of this study into the chromospheric layer of the solar atmosphere.

Although AIA images only possess limited spectral resolution compared to dedicated spectrometers, the latter consist of long-duration observations of coronal structures and at high enough spatial and temporal resolution to make gathering more in an automated manner very difficult. These AIA data are processed from level 1 to level 1.5, where the image is corrected for pointing and degradation of the CCD over time.

This image is then used in subsequent image enhancement techniques outlined below.

As previously mentioned, identifying coronal loops above background noise can be challenging. 'Background' noise in AIA images is a combination of diffuse blackbody radiation, charge spreading of electrons across neighbouring CCD pixel detectors, and the 'dark current' inherent to the detector without any imaged source. This is a combination of difficult viewing conditions and limitations by the physics of CCD-based image detectors, but the effects of this noise can be minimized with careful image enhancement techniques.

Multi-Gaussian normalization (MGN) as developed and outlined by Morgan & Druckmüller (2014) was chosen in this work to aid in the detection of coronal structures by means of highlighting local contrasts and enhancing their visibility. The geometries of these identified structures are subsequently examined by utilizing the coordinates of their cross-sections to the level 1.5 AIA images to construct intensity profiles. These calibrated images are prepared using the Sunpy (The SunPy Community et al. 2020) AIA prep routine, which applies a correction for instrument pointing at the time of the captured image, and registration which aligns each image with Solar north and rescales each image to ensure 0.6 arcsec per pixel coverage. Level 1.6 calibration, which additionally deconvolves the point spread function of each channel and replaces bad pixels with nearest neighbour values in each image, was considered too computationally expensive for the entire data set. MGN is a process by which Gaussian filters are applied to an image which is then combined with a weighted gamma transformed image, creating a composite image I. This is demonstrated in Figs 2(a) and (b), and expressed as

$$I = hC'_g + \frac{(1-h)}{n}\sum_{i=1}^{n} g_i C'_i, \tag{3}$$

where h is a global weighting value, C_g is the global gamma transformed image, and n is the number of unique Gaussian kernel widths used weighted by g_i weights. In the context of EUV observations, this technique has been used successfully in studies of Hi-C 2.1 mission data, compared to the data of the same time period and region as AIA, hence greatly enhancing the local contrast and reducing image blur caused by charge spreading and PSF (Williams et al. 2020a, b). This is done prior to image cropping to avoid introducing artificial boundary effects from applying MGN to blank regions adjacent to coronal structures.

Although MGN is used for highlighting local contrasts which is important for detecting geometries and reducing the effect of the point spread function, this can also magnify some pre-existing noise (e.g. dark noise). This can be alleviated by performing a time average over multiple MGN images taken in close succession. AIA captures images roughly 12 s apart (including exposure time), so although time averaging could lead to a 'blurring' of structures which change position or intensity rapidly in this short time window, the vast majority of coronal structures visible above the limb appear stable within the span of hours. The time-averaged data sets are created from images sampled sequentially to create one composite image composed of three images over roughly 36–40 s. This is repeated at 3 d intervals (see Section 2.4) resulting in approximately 1200 composite images per wavelength across the solar cycle.

It should be noted that MGN images are used as a 'tracing' layer to identify structural geometries. The images are then employed to reference the corresponding pixels in the corresponding level 1.5 data to determine intensity profiles for cross-sections. This is to avoid any effects that MGN filtering introduces which are non-physical or any alteration of the geometries of legitimate sources.

2.4 Constraining image data

As shown in Fig. 2(c), each image was cropped between the latitudes of 60 and 120 deg from the solar northern pole. The predominance of coronal holes and open plume-like structures increases outside of this range (Antonucci et al. 2020), which would lead to cross contamination of open plume like structures in the overall population of closed active region structures. These are likely formed and sustained by transient bright points (Madjarska 2019), connected to a more intricate network of magnetic structure at and below the photospheric layer (Morgan & Korsós 2022). Studies on the polar region and coronal plumes exclusively will be detailed in a forthcoming publication.

Limb images are constrained to an annulus of a fixed width between 1.05 and 1.10 solar radii (roughly 35 000 km). This height also allows for loops to be distinguished from their footpoints, and any emission close to the limb from visually indistinct and low lying coronal activity (such as from coronal moss and limb brightening effects), as well as minimizing dimming effects which occur from height. Additionally, the annulus allows for selection of unique coronal structures by utilizing a cadence determined by solar

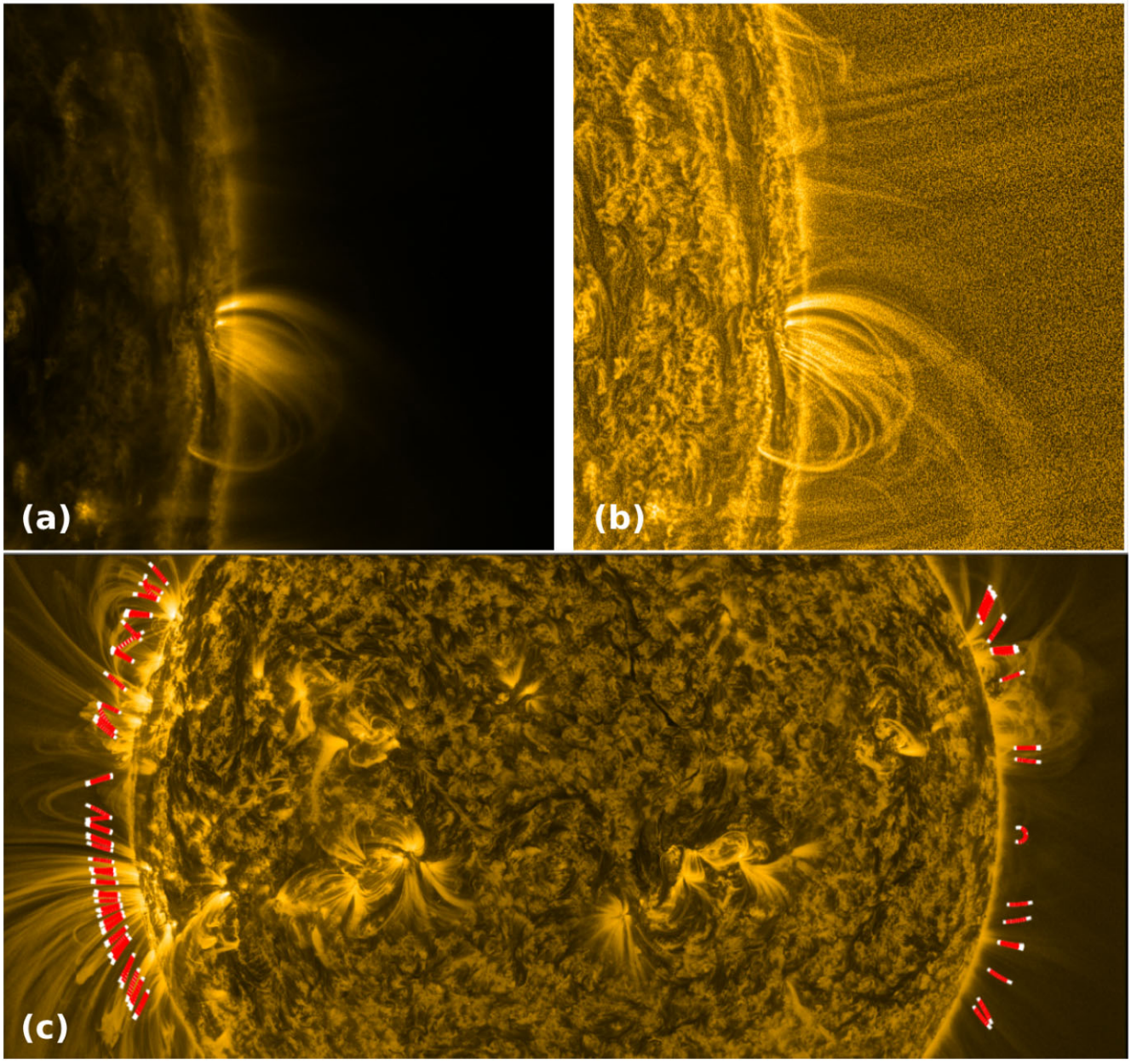

Figure 2. A section of the coronal limb and low disc as imaged in 171 Å (left) versus MGN processed level 1.5 (right). Contrasts in coronal structure are evident; local enhancements in the diffuse limb loop structure are highlighted with their structure visually preserved to greater height above the photosphere. (c) displays the fitting of structure segments on a cropped MGN image.

differential rotation. An example of this annulus fitted to a section of the limb is shown in Figs 3(a) and (b).

The resolution of the AIA instrument and the relatively diffuse nature of some coronal structures can contribute to uncertainties in detection of structural widths. This may result in the appearance of wider structures beyond just the thresholded power-law distribution resulting from equation (1), and subsequently affect a distribution of the overall population. In the event of multiple coronal structures overlapping within the line of sight, this could also result in difficulty distinguishing structures apart from one another, resulting in some spurious detections of coronal structures or repeated fitting in densely intense environments. This is a significant challenge for observational viewing campaigns in the solar corona, and an automated methodology is unlikely to be able to solve these issues without significant manual intervention. Therefore, this study adopted an artificial minimum distance (10 AIA pixels) between structural detections, which avoids the issue of overfitting but also cannot accurately fit all structures in a complicated environment. This does not prevent structures from crossing over one another, and exists to prevent overestimation of structures in dense regions or when imaging diffuse structures. This conservative approach reduces the amount of detections made, but increases the likelihood that detections represent unique structures.

Due to the variable lifetimes of coronal structures [which can range from hours to days or more depending on magnetic openness and degree of interaction with other nearby structures (López Fuentes, Klimchuk & Mandrini 2007; Nakariakov & Kolotkov 2020)], and the variable rotation rate of structures owing to differential rotation,

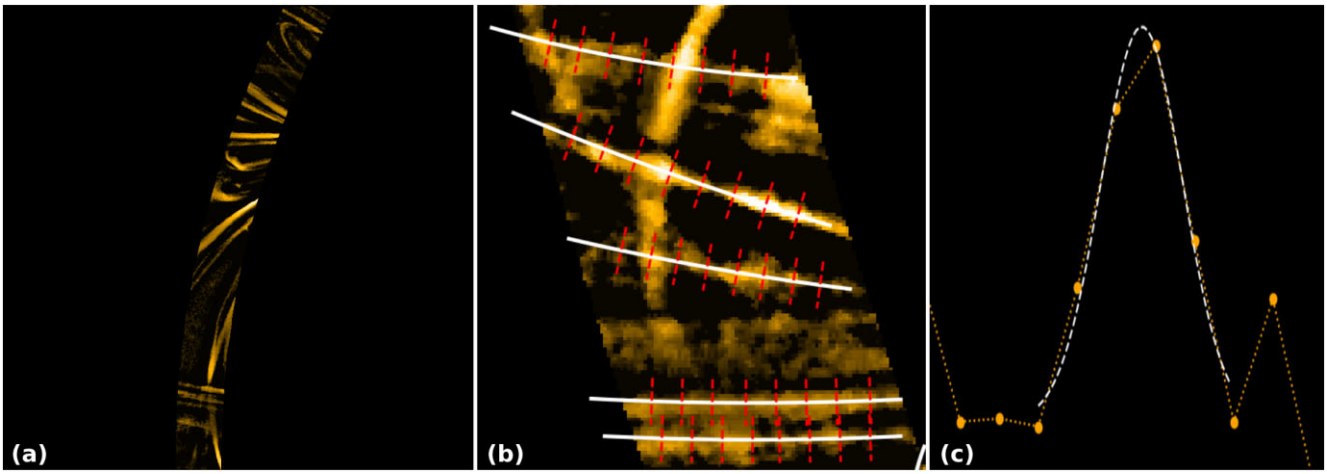

Figure 3. A section of the coronal annulus fitted to an MGN filtered 171 Å image and locally normalized and filtered to highlight coronal strands and other features. This image is used to trace geometry, and is not measured directly for structural properties. Panel (b) shows the structure fitting process across the fitted annulus, as well as the cross-sections chosen to produce average cross-section of fitted structure. Panel (c) shows background-subtracted cross-section and Gaussian function fitted to central peak, defining the observed geometry of the structure.

an optimal time cadence should be determined to prevent repeated detection of the same structures. Equation (4) details the relationship between latitude, distance from the inner annulus and time is found. Assuming that the x-coordinate position varies sinusoidally with time, and that a structure becomes visible once this x value is equal to or greater than the position of the inner annulus, the maximum time to clear the annulus is found to be

$$t = \frac{\tau}{\pi}\left(1 - \frac{r - r_1}{2(r_2 - r_1)}\right)\left(\frac{sin^{-1}(x_1) - sin^{-1}(x_2)}{cos(\theta_c)}\right), \quad (4)$$

where τ is the rotational period at latitude θ_c, r is the pixel position of the object, r_1, and x_1 and r_2, x_2 are the radial and Cartesian position coordinate of the inner and outer annulus at that latitude, respectively. For the aforementioned annulus, this equates to a time of 3 d or less for the highest latitudes, and so this was chosen as the time cadence between images in the data series. This dependence on the value of τ also restricts the latitude ranges chosen for the annulus.

As the width of a coronal structure is expected to vary with height to conform with the expansion of the coronal magnetic field (Klimchuk 2000), measuring structures at heights away from their footpoints may cause them to appear wider than would be seen closer to the photosphere. This may cause distributions of coronal widths to display a slightly stronger thresholding effect, by which narrow widths are seen less frequently than would be expected by a power-law relationship. This is not likely to significantly affect structures below two AIA pixel widths, as this is below the effective resolution of the instrument. As this expansion is not equally likely to affect all structures, this introduces some uncertainty with respects to width measurements, but is not likely to fundamentally change the shape of the distribution and their derived properties (such as power-law gradient).

2.5 Width measurements

In this work, coronal structural widths are defined as the derived measurement of the distance of a Gaussian profile fitted between measured minima of cross-sectional brightness profiles from identified structures. Though this work refers to coronal structures as generally Gaussian in cross-section, it should be noted that there are other possible interpretations of the morphology of coronal loops and other structures (Klimchuk & DeForest 2020). Given that a structure is assumed to arise when adjacent magnetic flux tubes are entangled and undergoes magnetic reconnection, and that the position and orientation of these structures can vary greatly from one point to another within the corona, there is nothing which guarantees that such cascades occur symmetrically, leading to irregularly shaped structures with non-Gaussian cross-sections. Furthermore, recent studies of MHD simulations of coronal structures performed by Malanushenko et al. (2022) suggest that some observed coronal structures are not cohesive bundles of flux tubes containing heated plasma, but are the result of diffuse, optically thin sheets of coronal plasma which can fold and appear as coherent structures. However, at this time there is not a body of observational analyses of coronal structures which support this conclusion that a large number of coronal structures are merely projection effects. Recent research performed upon Hi-C 2.1 sounding rocket data (Uritsky & Klimchuk 2024) does suggest that observed structures are not consistent with the aforementioned description of coronal veils. Additionally, it has been found that Gaussian profiles can be well fitted to coronal structures, even down to Hi-C resolutions, where it is possible to fit multiple Gaussian profiles to single cross-sectional profiles due to the high pixel resolution of the instrumental data (Williams et al. 2020b, 2021). As such, the work in this paper will assume structures conform to a symmetrical, Gaussian profile.

Thus, if coronal structures are considered to possess a Gaussian cross-sectional density profile *e(x)*, then the intensity of emission as a function of x displacement from the centre of the profile can be described as

$$e(x) = a.\exp - \frac{(x - x_p)^2}{2w^2}, \quad (5)$$

where a is the height of the Gaussian profile, x_p is the central position of the loop profile, x is the position away from the central position, and w is the standard deviation of the Gaussian profile.

In many studies of coronal loops, identification and tracing is performed manually, or semi-automatically in pre-defined regions of interest. To fully utilize the extent of the AIA data set over Cycle 24, it is necessary for identification and tracking to be performed autonomously upon an image. In this case, the investigation of coronal geometry utilizes custom software to process and analyse

thousands of AIA EUV images in the four wavelengths mentioned previously. Here, a modified version of the OCCULT algorithm (OCCULT; Aschwanden 2010), OCCULT-2 (Aschwanden, De Pontieu & Katrukha 2013), is employed which performs well in coronal loop detection in multiple EUV wavelengths (see Data Availability section for links to source code).

The annulus-based approach can constrain some issues of complex loop geometry by fitting shorter, well-defined loop segments, but cannot account for closed structures which re-enter the annulus at a different location. An example of a region of traced loops on a region of a composite MGN annulus is shown in Fig. 3(b). This methodology favours quasi-radial structures which cross the annulus from one side to the next, and so may select less structures which enter at a shallow angle and do not pass to the other side. A modified method which places more weight on shallower geometry angles as a primary or secondary pass might detect more of these shallower, longer structures.

Once a loop segment is traced across the cropped annulus, eight equidistant intensity cross-sections are taken from the original level 1.5 data and used to construct a mean average intensity profile. Local background is estimated by linear interpolation between local minima, and a Gaussian profile fitted to the reduced profile to estimate width. An example profile is shown in Fig. 3(c).

2.6 Uncertainties of width power laws

The resulting power-law gradient will be used to compare different regions, time periods, and wavelengths of coronal structural populations, thus the uncertainty will be derived from statistical interpretations of individual width uncertainties associated with the fitting of individual Gaussian profiles to structural cross-sections. Uncertainty in width measurements originates in the closeness of the fit to an optimal Gaussian profile utilizing a least squares best-fitting algorithm. Each bin of this histogram is an equal distance in log space, with the horizontal axis being structural width in AIA pixels, while the vertical axis is occurrence frequency. Assuming that each width is normally distributed within its uncertainty, the probability that a width falls within the range of widths for a given bin can be calculated. The mean average of the probabilities for all of the widths in a bin constitute the percentage uncertainty for that particular bin, meaning the numerical error is equal to the uncertainty probability p multiplied by the number of structures in that bin N. A standard error of $\sqrt{n}$ is also applied as an additional 'safety' buffer. The final uncertainty for each bin frequency is then represented by equation (6):

$$\Delta N = \bar{p}N + \sqrt{N}, \tag{6}$$

where ΔN is the uncertainty of the frequency, $\bar{p}$ is the mean average probability of falling outside of a bin threshold, and N is the total frequency of coronal structures within a bin.

2.7 Latitude measurements

Latitudes are recorded from 0 to 180 deg, equivalent to the Stonyhurst heliographic coordinate system (Thompson 2006), where latitude L is equal to the coordinates Φ, Θ, which are horizontal and vertical displacements from the solar prime meridian and the equator, respectively. In this work, all latitudes are quoted as magnitude displacements from the north pole, i.e. $\Theta = \pm 90$.

Table 1. Loop frequency by wavelength and period.

Wavelength (Å)	Rise	Peak	Decay	Total
171	11 694	28 140	34 369	74 203
193	8584	23 466	27 300	59 350
211	7287	19 848	22 158	49 293
304	1492	3346	3178	8016

3 RESULTS

3.1 Structural widths

The frequency, defined as the total number of structures detected by wavelength, is demonstrated in Table 1 and Fig. 4. These describe distribution of the width of structures detected in all four wavelengths throughout the solar cycle by phase and in total. Note that these distributions include those measurements detected below the 2 pixel resolution limit of the AIA instrument, and includes the prominent 'spikes' between 0.3 and 0.4 pixels seen in all wavelengths in Fig. 4. This is an artefact of Gaussian fitting between narrow pixel ranges and will be ignored (see more below).

More detailed examinations of structure width populations and their power laws can be made by restricting the sample to the range of 2.7–5 pixel widths. Hence the physical and observational effects described in Sections 1.2 and 2.4 are minimized, and a more targeted examination of power-law gradient slopes can be carried out. The upper limit of 5 pixels is determined by the sensitivity of ranges beyond this point to small number statistics, which would result in very small numbers of structures altering the overall measured gradient of the profile. Results in this range are presented in Table 2 and Fig. 5. The gradients of these distributions are estimated by fitting a power law across the centrepoints of each bin in this range by means of linear regression. This results in a thresholded power-law distribution of observed structure widths, indicating a log versus log relationship between width and frequency for structures within a given time period. Subsequently, this relationship is indicative of a probability distribution of structures observed across these time periods. The gradients within different periods across each wavelength and time period within the range of 2.7–5 pixels is outlined in Table 3.

Consider the Rise, Peak, and Decay periods across all wavelengths in Fig. 5. Within the Rise period, gradients of structure populations are generally less steep than those seen in the decay phase, but are equally or more steep than gradients seen within the Peak phase. This can be seen in 171 Å, with the magnitude of the rise gradient being 1.67 ± 0.09, and the magnitude of the Peak and Decay periods being 1.63 ± 0.07 and 2.06 ± 0.08, respectively. This is similarly mirrored in 193 and 211 Å, with 304 Å demonstrating a significantly steeper gradient in the Decay phase (-5.51 ± 0.33) than would be expected from trends seen in other wavelengths. However this is likely due to low numbers (<100) of high width (>4 pixels) affecting the slope of the power law, as well as a greater instrumental sensitivity of the 304 Å filter to low temperature structures which are less abundant in the imaged region.

Overall, these distributions display a difference in power-law gradients between wavelengths for structures captured throughout the entire solar cycle, with gradient magnitudes of 1.81 ± 0.06, 2.05 ± 0.05, 2.89 ± 0.07, and 3.86 ± 0.13 for 171, 193, 211, and 304 Å structures, respectively.

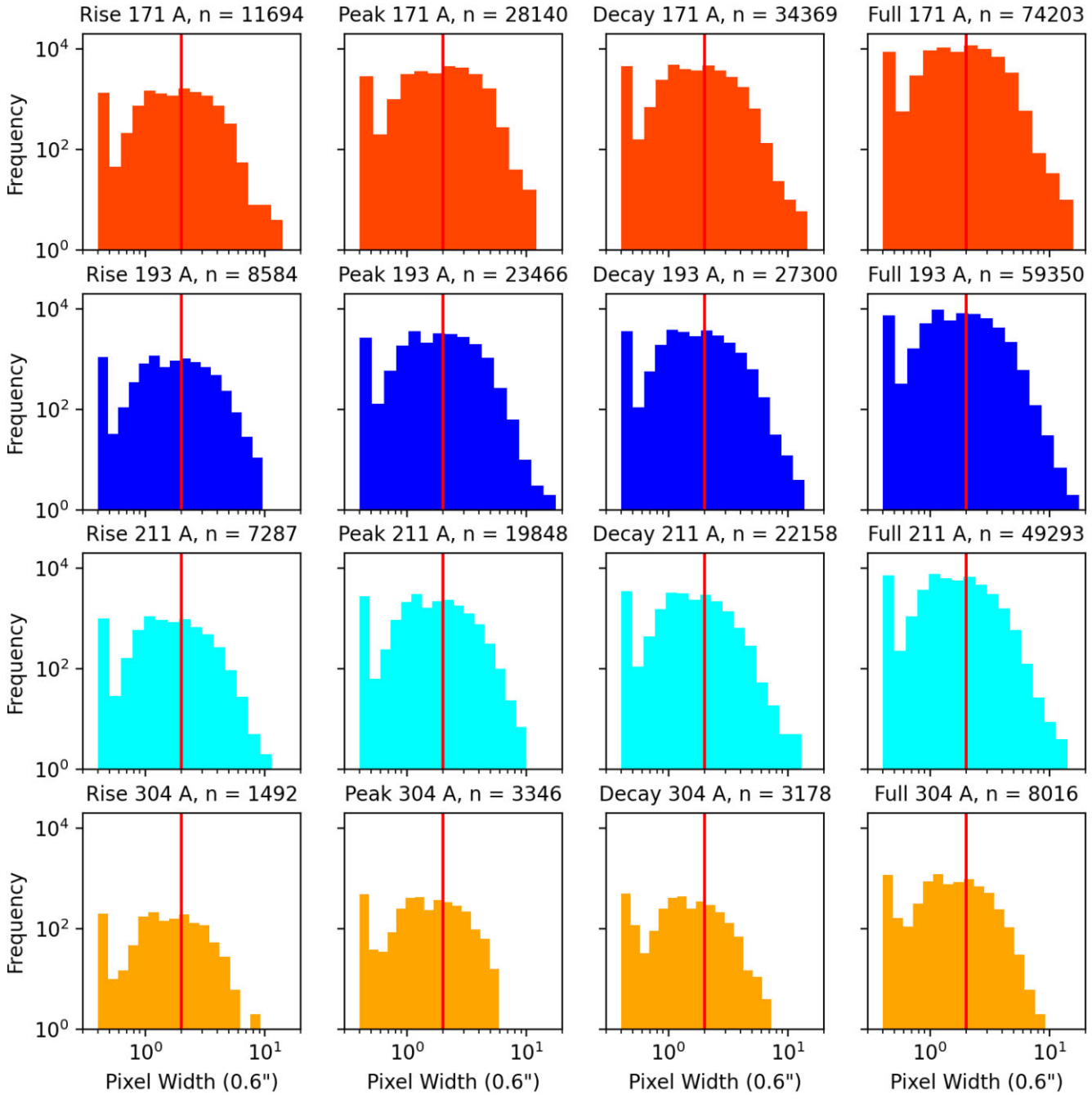

Figure 4. Width occurrence frequency diagram for all AIA pixel widths. The 'spike' on the left-hand side of each figure is an artefact of Gaussian fitting across narrow peak ranges. The red vertical line indicates peak of threshold distribution at 2 pixels. Both axes are logarithmic.

Table 2. Loop frequency by wavelength and period. Loop widths between 2.7 and 5 pixels.

Wavelength (Å)	Rise	Peak	Decay	Total
171	2730	7787	6890	17 430
193	1774	5509	4965	12 280
211	1124	3302	2840	7285
304	234	495	340	1071

3.2 Latitude frequency and asymmetry of coronal structures

The extent to which coronal structures exhibit any latitudinal asymmetry in different periods of the solar cycle or in different wavelengths could provide insight into the relation between the level of solar magnetic activity and the relative population of coronal structural populations. Possible asymmetry is examined in more detail in Fig. 6, where the total and average occurrence frequencies in the Northern and Southern hemispheres for observed coronal widths is shown. Comparing this to Fig. 1 (which examines the total sunspot frequency by hemisphere for the same cycle), the overall activity

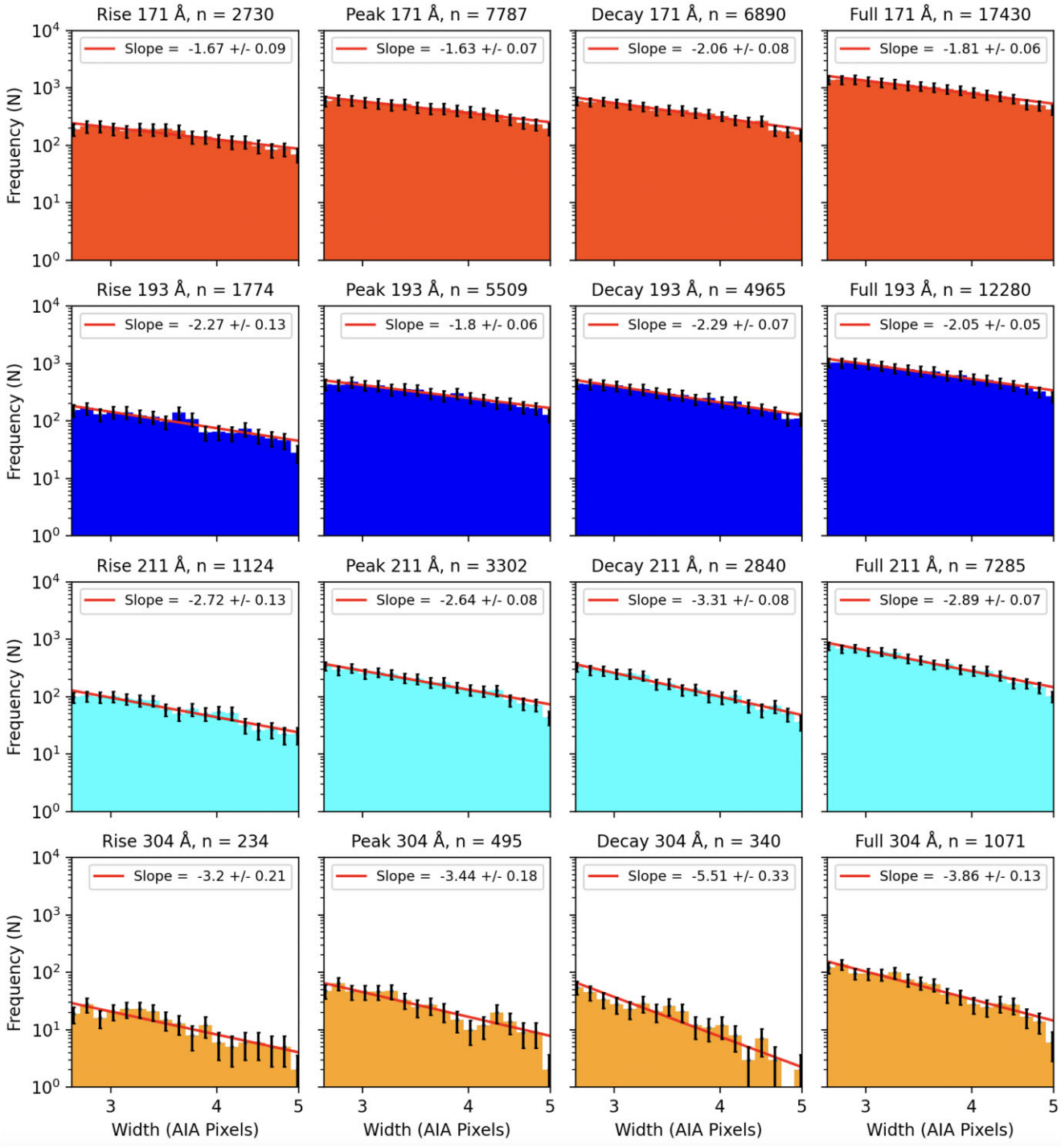

Figure 5. Width occurrence frequency diagram with a cut-off between 2.7 and 5 pixel widths. At this level the differential gradient is closer to the ideal SOC case of around -1.5. Variation throughout solar cycle is persistent through different wavelengths but shows more consistency than the wider range. Both axes are logarithmic.

is biphasic. The Northern hemisphere (blue) population is greater on average throughout the cycle than the Southern hemisphere; however, the Northern hemisphere peaks earlier and begins decaying sooner after the start of the 'peak' phase. In contrast, the Southern hemisphere only peaks in activity towards the start of the decay phase. Subsequently, both hemispheres decay to negligible activity by the end of cycle 24.

Fig. 7 demonstrates the relationship between solar activity time period and latitudinal frequency for the population of widths across each wavelength. The fraction of structures which appear in the Northern hemisphere is indicated by N Loops, and the North–South Index (see equation 2) is given by an NS Index for each wavelength. Index and northern predominance fraction values provided for sunspots and each wavelength in Table 4. Consider the 171 Å results

Table 3. Width frequency power-law gradient by time period and wavelength – 2.7–5 pixel widths. Gradient is measured as the ratio of the log of structure width versus frequency.

Wavelength (Å)	Rise	Peak	Decay
171	-1.67 ± 0.09	-1.63 ± 0.07	-2.06 ± 0.08
193	-2.27 ± 0.13	-1.80 ± 0.06	-2.29 ± 0.07
211	-2.72 ± 0.13	-2.64 ± 0.08	-3.31 ± 0.08
304	-3.20 ± 0.21	-3.44 ± 0.18	-5.51 ± 0.13

(top row, Fig. 7). This demonstrates a small but detectable variation from northern dominated structure populations in the Rise phase: 0.59 followed by a switch to a southern dominated population (0.46) in the Peak phase, and then another change towards northern lead populations in the Decay phase (0.51). These suggest a consistent degree of variation for coronal populations between periods, although the overall changes are small, but observable. These figures mirror other indicators of solar activity i.e. sunspots as shown in Fig. 1.

It should be noted that the asymmetry arises from the two hemispheres displaying different profiles of activity across the solar cycle, rather than the two cycles simply being totally out of phase or of one demonstrating a smaller amplitude than the other. The Northern hemisphere reaches a maximum earlier in 2012, resulting in a northern lead Rise phase, with the predominantly southern Peak period caused by a more sudden rise of southern lead activity combined with the slowly decaying northern activity.

Taken together, these asymmetries of coronal populations can be described as a double-peaked distribution centred at roughly 70 and 110 deg from the northern pole (corresponding to the active region belts), which rise and fall in activity at different times. These values and the profiles of the population display a bifurcation of the overall distribution, although overall there is parity for population quantities between hemispheres, the phases in which one hemisphere is dominant varies in time.

The solar magnetic field is expected to be north driven in solar cycle 24 based on the southern driven field in Cycle 23 and the 11 yr period of the solar magnetic cycle (Babcock 1961). However, the results of latitude distribution of active region coronal structures versus time indicate an earlier peaking but extended decaying of coronal activity in the north, and a delayed peaking but accelerated decaying of activity in the south. The highest period of overall sunspot activity occurs due to southern activity rather than that of activity in the hemisphere which dominates the cycle as a whole, hence showing that the phenomenon of hemispheric asymmetry is more nuanced than simply a North versus South predominance per cycle. This view is supported by other examinations of the solar cycle conducted with synoptic line-of-sight magnetograms (Janardhan et al. 2018).

As expected, direct comparison of coronal width frequency in Northern versus Southern hemispheres to corresponding sunspot numbers yields a strong positive correlation. This is seen in Fig. 8, which compares normalized hemispheric sunspot occurrence frequencies in raw and smoothed (monthly average) distributions with measured coronal structure equivalents. A lag is seen between some individual peaks of coronal width frequency, but is not consistently before or ahead of corresponding sunspot peaks and likely can be attributed to the difference in where these statistics are collected i.e. limb loops are measured in two locations perpendicular to line of sight and sunspots are detected across the entire solar disc.

There are underlying commonalities between structure populations across different wavelength regimes, indicating that despite being composed of different plasma populations, the underlying conditions required to produce these structures are similar. Hence, Maunder butterfly diagrams (Hathaway 2005) were chosen to compare the spatial distributions of coronal width populations with sunspot figures, as seen in Fig. 9, using the Royal Belgian Observatory SILSO (Sunspot Index and Long-term Solar Observations) (SILSO World Data Center 2020) daily North and South sunspot coverage figures.

A line of best fit was calculated for each hemisphere of the sunspot butterfly diagram (top) by means of liner regression between the cells of highest area coverage (yellow pixels). It is seen that coronal widths bear considerable visual similarity to the sunspot distribution – following a similar if slightly broader distributions (40–30 deg displacement from the equator at the start of the solar cycle, to 15 deg displacement at the end of the cycle), consistent with Spörer's Law (Ivanov & Miletsky 2014). In particular, loops are seen across the whole range of latitudes at all periods, though they are concentrated at positions which correspond to sunspots.

Given the intrinsic link between coronal loops and sunspots, it should be expected that coronal loop frequency is strongly correlated to sunspot frequency; this relationship is examined in Fig. 8, where the normalized difference of sunspots by hemisphere is compared to the normalized difference of loops by hemisphere.

To quantify the comparison between the monthly averages of coronal loops and sunspots, a cross-correlation was calculated between the overlapping date ranges (2010 July 1 to 2019 December 30), with the standard cross-correlation formula:

$$C_{ab}(\tau) = \sum_{i=1}^{n} a(n+\tau) * \overline{b(n)}, \tag{7}$$

where C_{ab} is the cross-correlation of the functions a and b, with time delay τ. $\overline{b(n)}$ is the complex conjugate of the function b(n). The results of this cross-correlation are displayed in Fig. 10. In this case, a is the function of normalized north minus south sunspot occurrence frequencies, and b is the function of normalized north minus south loop occurrence frequency for 171 Å populations. This cross-correlation is optimal at the 114th displacement value, compared to series length of 116, indicating that the two series are almost perfectly aligned. Therefore, the series of monthly average hemispheric sunspot counts and coronal widths are best aligned without any delay. This is despite some apparent lags seen between spikes of normalized frequency in either series; the lags are either before or after corresponding spikes in sunspot count, though these mostly occur in the decay phase, when there are likely to be low overall counts of both sunspots and coronal structures, making the N-S average more liable to larger variation.

3.3 Correlation of observed width and latitude

To quantify any potential correlation, a Spearman rank correlation coefficient (SRCC) and associated p value has been determined for the width versus latitude of each loop in the range of 2–12 pixel widths for each wavelength, displayed in Table 5. The standard equation for SRCC is shown as

$$R_s = 1 - \frac{6\sum d_i^2}{n(n^2-1)} \tag{8}$$

Here, R_{s} is the correlation coefficient, n is the number of total observations, and p is the standard p-value test based on the Student t-distribution. $\sum d_{\mathrm{i}}$ is the sum of the difference in ranks of each observed loop in width and latitude.

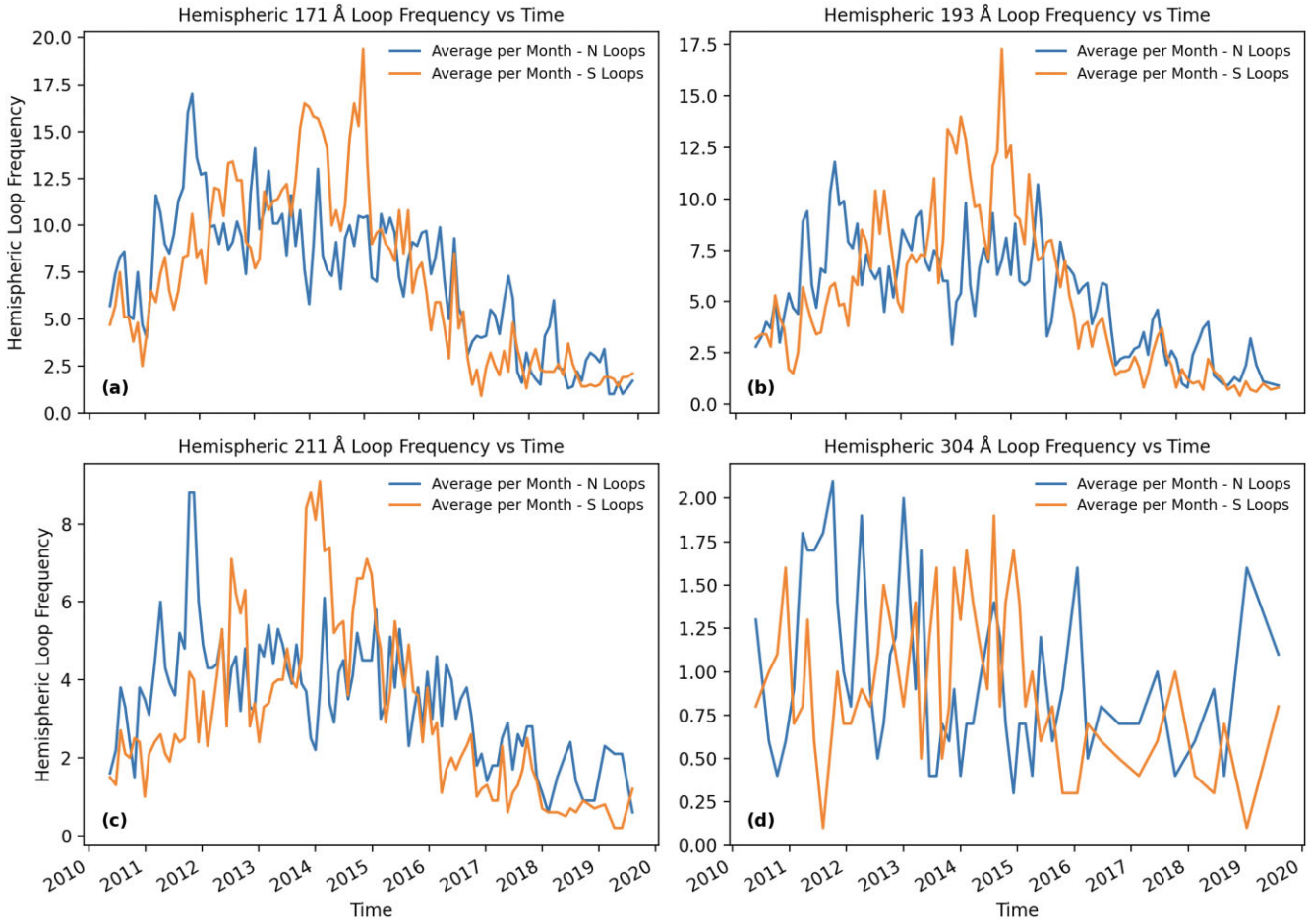

Figure 6. Hemispheric structure occurrence frequency versus time for all wavelengths. Blue indicates northern activity, and orange indicates southern activity. The dots and lines indicate loop counts by day and monthly average, respectively. All loops are above 2.7 pixels in width.

Values of R_s indicate a very low likelihood of any correlation between loop width and position, approaching a perfect lack of correlation to within 0.05 and a large sample size. Values of p similarly increases the confidence that the observed lack of correlation is not a coincidence of the data set. The high value of p in the 193 Å distribution is likely due to the relatively small value of R_s (-0.0026 for 193 Å compared to 0.0164 for 171 Å). Such a small correlation would require a very large sample size to demonstrate statistical significance. Therefore, it is unlikely that any correlation might be established between width and latitude based on the information gathered in this data set in any wavelength.

This indicates a general similarity in the populations of coronal structures imaged regardless of their viewed latitude, and that footpoints at each latitude is equally as likely to produce loops of any coronal width as other latitudes. This could indicate that changes in observed structural width and the required conditions for forming larger loop structures may not vary by latitude as much as by time period. Overall, despite some small variance in structure width across latitude and time period, analysis of latitude versus width indicates that it is a poor indicator of the width of a loop at any time period. At the present time, there is no evidence to suggest any relationship between observed structure width at the limb and latitude of occurrence.

4 DISCUSSION AND CONCLUSIONS

The coronal structures described in this work represent coronal plasma populations at differing temperatures and time periods. It was anticipated that investigating changes in coronal structure widths and latitudes across solar cycle 24 would allow for more detailed insight into the possible determination of SOC gradients in, and asymmetry of the corona and chromosphere over time, and that trends might be identified which had previously escaped detection. This relied upon the comprehensive analysis of 171, 193, 211, and 304 Å filters of SDO's AIA instrument. The periods of Rise, Peak, and Decay were defined to describe distinct phases of solar magnetic activity, corresponding to the times between 2010 May 13, 2011 November 15, 2014 November 15, and the end of 2019, respectively.

Structures were isolated above the limb within a fixed annulus, with segments traced automatically at a rate of one image per 3 d. Gaussian profiles were fitted to cross-sectional intensity values. From these profile measurements, over 50 000 structures were measured in all wavelengths above 2.7 pixel widths (the limit of confident width detection imposed by instrumental constraints).

From the resulting extensive data set, analysis of possible width and latitudinal variation was performed. Coronal structure widths were analysed by compiling the width of all loops between 2.7 and

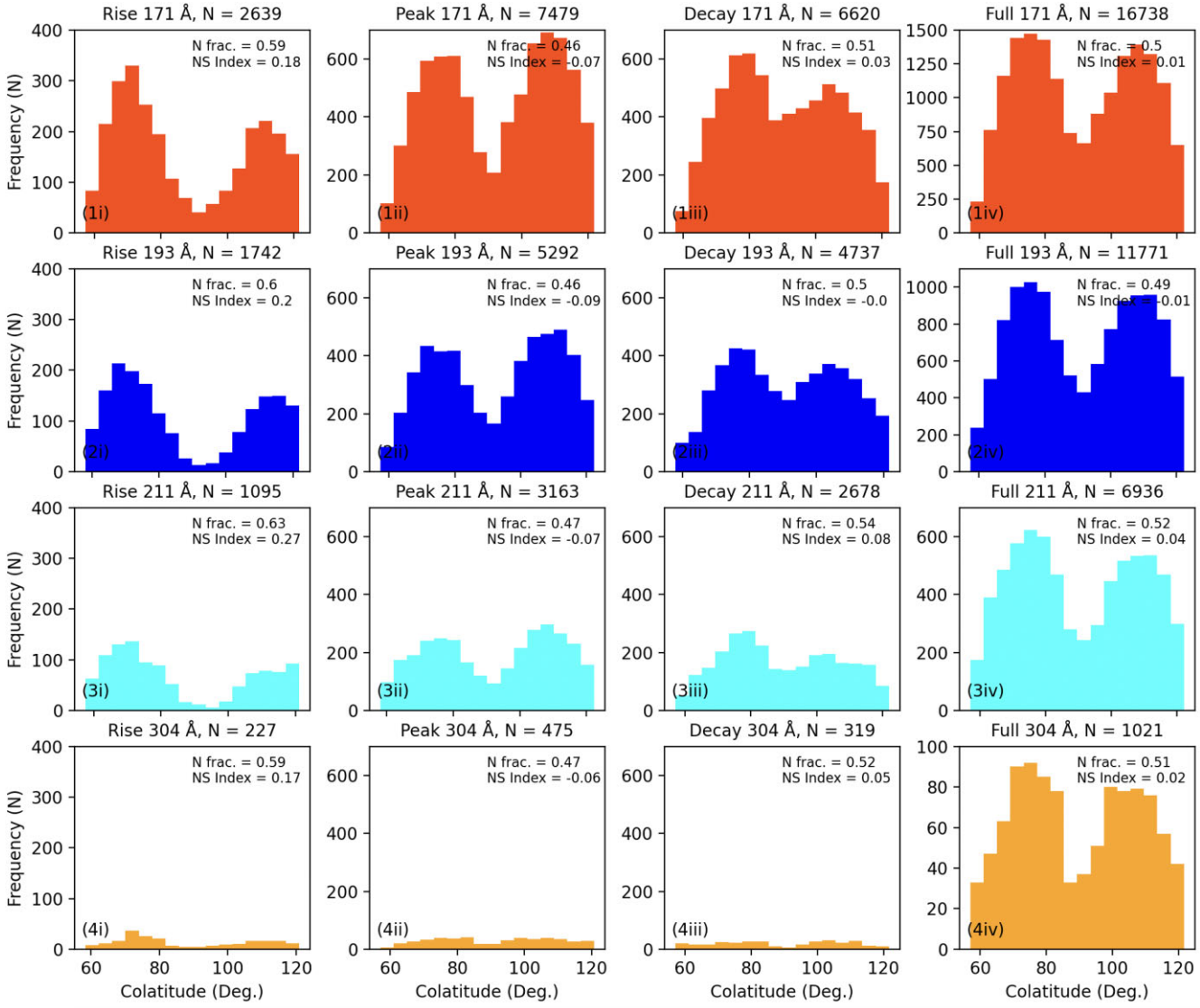

Figure 7. Latitude occurrence frequency diagram for all coronal loops above 2.7 pixel widths by wavelength and solar cycle activity period. Total numbers vary slightly from those presented in Fig. 5 due to differences in binning range coverage.

Table 4. North–South loop asymmetry across three time periods. The left column F represents Northern hemisphere loops as a fraction of total loops. The right column A represents N-S loop asymmetry index for chosen period and wavelength.

Wavelength	Rise		Peak		Decay	
	F	A	F	A	F	A
Sunspots	0.68	0.36	0.37	−0.27	0.73	0.46
171 Å	0.59	0.18	0.46	−0.07	0.51	0.03
193 Å	0.6	0.19	0.45	−0.09	0.5	0.00
211 Å	0.63	0.26	0.47	−0.07	0.54	0.08
304 Å	0.59	0.17	0.47	−0.06	0.52	0.05

5 pixels separated into wavelengths and subsequent populations in the rise, peak, and decay period (as well as an aggregated full time period for comparison). The power-law gradient of the produced distribution was compared to both theoretical SOC distributions (-1.5 for fractal diffusive SOC) and those measured by other studies of on-limb coronal loops measured in 193 Å (-2.7 to -3.1 for Zhiming et al. 2019 and Aschwanden & Peter 2017). These distributions were found to vary across the solar cycle, increasing in magnitude throughout these distinct periods; for example, -1.67 ± 0.07, -1.63 ± 0.08, and -1.81 ± 0.06 for rise, peak, and decay in 171 Å, respectively. This trend indicates that observed loop structures appeared to change over time, with less wide structures and more narrow structures present within width distributions as solar magnetic activity became less intense. This trend was mirrored across multiple wavelengths, but 171 Å populations were generally steeper than 193 Å, and 211 Å were significantly steeper than both 171 and 193 Å. Chromospheric 304 Å populations were much less well populated than other wavelengths, and it was challenging to determine the gradient of their power-law slopes.

This research has revealed two things: (i) that loop width power-law distributions change throughout the solar cycle, indicating a possible change to the rate non-linear dissipative events thought to produce coronal loops at their footpoints in the photosphere, and (ii) that these differences are consistent between wavelengths.

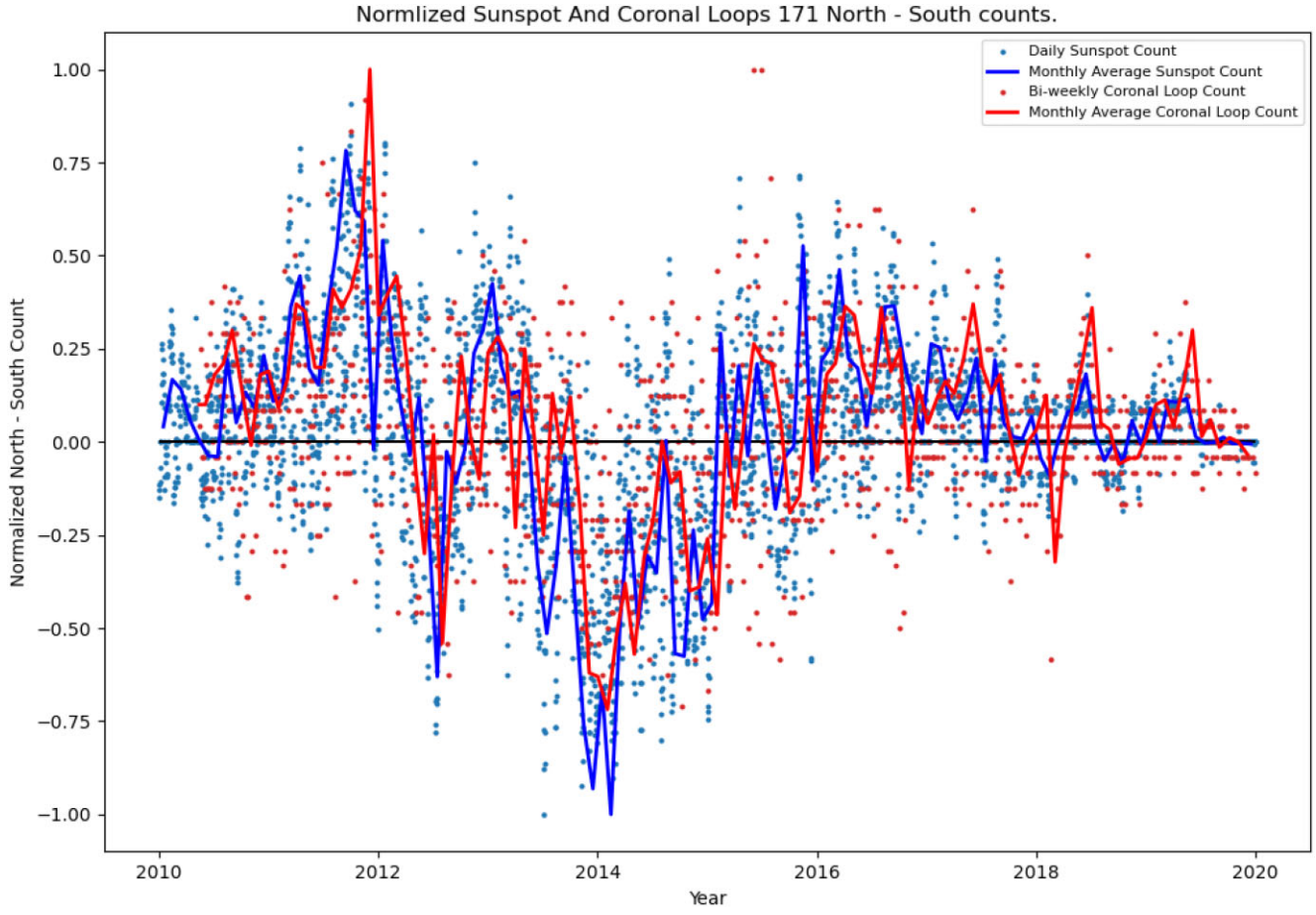

Figure 8. Diagram of normalized hemispheric difference (north minus south) for 171 Å loops and daily sunspot figures versus time over the solar cycle 24. The lines indicate the monthly averages for both. Sunspot data are from SILSO (SILSO World Data Center 2020).

The F.D estimation of -1.5 for the value of the power-law gradient of the distribution is based upon the scale invariability of the distribution of the size of events across many orders of magnitude, occurring with perfectly efficient exchanges of energy. That some of the observed distributions follow power-law profiles with gradient values approaching -1.5 is evidence that this statistical principle can apply to the distribution of coronal structural widths, though discrepancy is to be expected. These discrepancies can be categorized as either observational or physical. Of the two, physical discrepancies are useful for providing information to the physics within the structure forming regions, and observational discrepancies must be controlled for when possible. As SOC is a statistical model representing ideal cascading exchanges of energy in a uniform grid of arbitrary dimensions, with no direct physics, it is used as an approximation of the distributions and statistics that such a system may result in.

Observational discrepancies are caused by limitations of the equipment such as CCD charge spreading, causing the intensity 'peak' seen in the overall distribution in Fig. 4 at 2 pixels, and may also result in steeper than expected gradients as narrower structures are misidentified as wider structures in lower pixel ranges. Another observational complication is line-of-sight effects such as structure conflation, by which multiple structures overlap within the line of sight and are subsequently misidentified, and can cause thresholding effects (see equation 1). Additionally, background subtraction can result in wider and dimmer structures as being detected as narrower than they are in reality. As there is generally little correlation between coronal structural width and observed intensity (Klimchuk & DeForest 2020), this can potentially curtail distributions at the wider ranges (>4 pixels). These effects can be mitigated by making repeated observations, and comparing results seen in various periods of time. This allows for observational effects to remain consistent in all measurements, meaning that any changes in the resulting gradients are more descriptive of discrepancies caused by physical processes than aforementioned observational effects.

Physical variations could be caused by effects analogous to those which are known to affect SOC-like populations. These include but are not limited to (i) limited size scaling effects which curtail the size distribution available to cascade over, (ii) quenching effects which removes energy in a way which does not contribute to further cascading, and (iii) variations of dissipation time-scales which alter the amount of time available for energy to dissipate throughout the system. Additionally, other SOC assumptions like stochastic addition and that the local or global critical threshold is constant may not be accurate representations of structure forming regions in all cases. Variation in observed parameters (such as width distributions) across solar cycle could in part aid in describing the fundamental effects such as reconnection rates and mechanisms which influence the formation of coronal structure. Differing gradients will necessitate differing rates of reconnection events which then generate observable structural widths, which must be consistent with predicted values. Observed variations from ideal FD-SOC could indicate that physical

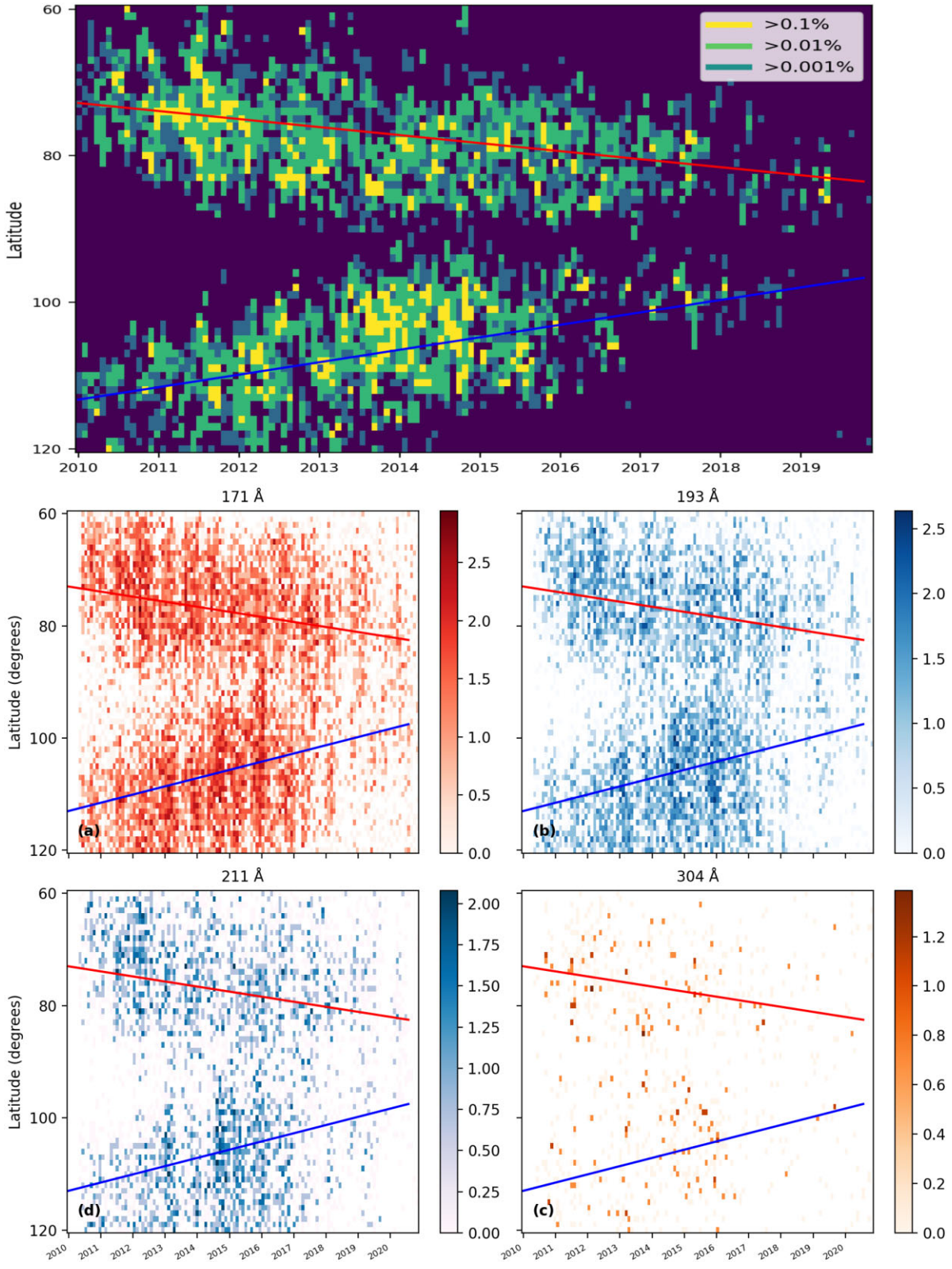

Figure 9. Top: sunspot umbra area coverage by latitude and time, bottom: coronal structural occurrence frequency (between 2.7 and 5 pixel widths) by latitude and time. Colour maps correspond to e^x frequency for each position indicated as shown on vertical bar. A line of best fit is calculated for sunspots across yellow pixels (greater than 0.1 per cent coverage) and plotted over coronal populations in each hemisphere.

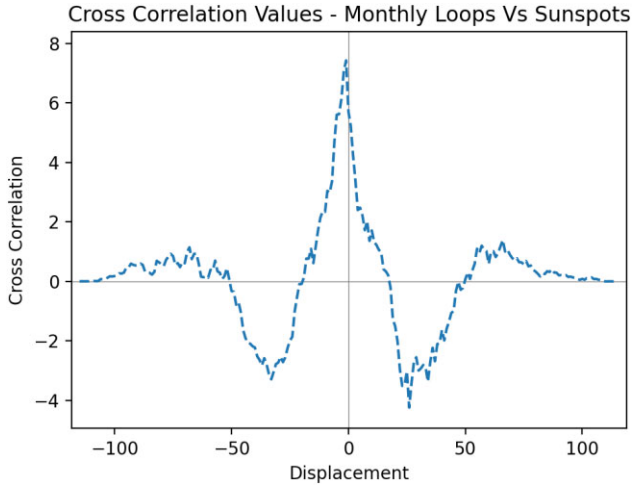

Figure 10. The cross-correlation of monthly average hemispheric sunspot count difference and coronal loop hemispheric frequency difference. The peak value of the cross-correlation occurs at position 108, corresponding to the length of the shortest sequence.

Table 5. Table demonstrating SRCC results for loop width versus latitude for each wavelength, showing the R_s value, p value, and n number.

Wavelength (Å)	R_s	p	n
171	0.0164	0.0063	27 847
193	−0.0026	0.7248	19 017
211	−0.0196	0.0378	11 186
304	0.0450	0.07504	1567

processes responsible for the appearance of coronal structures may be less similar to the ideal assumptions, particularly in later periods of the solar cycle than in the earlier, more active periods. The value of the power-law slope of the frequency distribution of loop widths $D(w)$ is expected to be analogous to the same power-law gradient of cascading events α_s taking place within the emerging region assuming that principles of SOC apply to the phenomenon of coronal loops.

Similarly to loop widths, loop latitudes were recorded and compiled. These latitudes were also divided into rise, peak, decay populations, and the distributions examined (see Fig. 7) These distributions revealed asymmetries in coronal and chromospheric loop populations in Northern and Southern hemispheres which varied throughout the solar cycle, but which remained relatively consistent between wavelengths; Northern hemispherical fraction is 0.50 for 171 Å, 0.49 for 193 Å, 0.52 for 211 Å, and 0.51 for 304 Å. While these fractions are similar across each wavelength, there is significant variation within the solar cycle, up to 14 per cent between Rise and Peak phases.

Also described was the relationship between the observed latitude of coronal loops and time, compared to sunspots within a Maunder butterfly diagram within Fig. 9. These diagrams indicate a strong relationship between the latitudes that sunspots emerge and the latitudes that coronal loops can be observed, as these populations were matched by the same trend lines in both hemispheres in all populations.

Following this, analysis of the relation between loop width and latitudinal position was performed within each of the periods of study mentioned previously. The purpose of this analysis was to examine the relation between coronal activity and latitude. This is examined statistically by means of a test of the correlation coefficient of width and latitude for each loop recorded above 2 pixels. The results (Table 5) show an R_s value magnitude of less than 0.05 for every wavelength. This indicates that no meaningful relation can be determined between loop latitude and width independent of time period, and that the conditions at each latitude do not vary substantially with regards to coronal loop formation.

4.1 Future work

Further investigations will include more detailed examination of loop populations present in existing and future data sets, such as examination of historical observations from the Solar and Heliospheric Observatory (SOHO) (Domingo, Fleck & Poland 1995) Extreme-ultraviolet Imaging Telescope (EIT) (Delaboudinière et al. 1995), and solar cycle 25 with the ongoing SDO AIA and targeted studies of active regions with Solar Orbiter's (Müller et al. 2020) Extreme-Ultraviolet Imager (EUI) (Rochus et al. 2020). This will be of use in understanding how the coronal response varies from one cycle to the next. Additionally, examining further the nature of structural width gradient changes and how they may relate to specific heating mechanisms within/without active regions and across different periods of the solar cycle may be useful as a probe of exact heating mechanisms and thresholds.

Analyses of coronal latitude occurrence could be improved by quantifying gradients for slopes demonstrated in Fig. 9 for each wavelength. This will aid in determining if and to what extent the different populations occur in differing latitude ranges and if they migrate with the same rate towards the solar equator across the solar cycle. West versus East loop occurrence could be compared to the total sunspot figures for North–South asymmetry to examine the slight lags seen in Fig. 1 and confirm if they were caused by the difference between positions of sunspots and limb loops.

Additionally, the current quantity of structures detected in this range is limited owing to the necessities of employing a conservative approach to the data sets. This method could be improved by means of machine-learning-based image segmentation for instance, hence producing a wider possible range of statistics such as structure broadening or DEM temperature/density estimations as possible examples. The sensitivity of the 10 pixel blocking radius around confirmed structures could also be investigated, and the over versus underestimation of various radii could be quantified in line with an improved future algorithm. Studies of profiles in each hemisphere to study whether differences in the observed behaviour of the solar cycle are reflected in observational statistics of the solar structures (such as width and frequency as shown in this paper) could then be performed.

ACKNOWLEDGEMENTS

This research was funded by the University of Central Lancashire as part of the Jeremiah Horrocks Institute Postgradute Research program fund, utilizing data made available by NASA, the ESA, and SILSO.

DATA AVAILABILITY

The data underlying this article and the software used is freely accessible from the UCLAN Data Archive, at https://doi.org/10.17030/uclan.data.00000377.

REFERENCES

Antonucci E., Harra L., Susino R., Telloni D., 2020, Space Sci. Rev., 216, 117
Aschwanden M. J., 2010, Sol. Phys., 262, 399
Aschwanden M. J., Peter H., 2017, ApJ, 840, 4
Aschwanden M., De Pontieu B., Katrukha E., 2013, Entropy, 15, 3007
Babcock H. W., 1961, ApJ, 133, 572
Bak P., Tang C., Wiesenfeld K., 1987, Phys. Rev. Lett., 59, 381
Bak P., Tang C., Wiesenfeld K., 1988, Phys. Rev. A, 38, 364
Bell B., Glazer H. G., 1958, Smithsonian Contributions to Astrophysics. Smithsonian Archives, Smithsonian Institution
Beveridge C., Priest E. R., Brown D. S., 2004, Geophys. Astrophys. Fluid Dyn., 98, 429
Brooks D. H., Warren H. P., Landi E., 2021, ApJ, 915, L24
Carbonell M., Oliver R., Ballester J. L., 1993, A&A, 274, 497
Chitta L. P. et al., 2022, A&A, 667, A166
Dahlburg R. B., Einaudi G., Ugarte-Urra I., Rappazzo A. F., Velli M., 2018, ApJ, 868, 116
Delaboudinière J. P. et al., 1995, Sol. Phys., 162, 291
Domingo V., Fleck B., Poland A. I., 1995, Sol. Phys., 162, 1
El-Borie M. A., El-Abshehy M., Talaat S., Taleb W. M. A., 2012, Astrophysics, 55, 127
El-Borie M. A., Abdel-halim A. A., El-Monier S. Y., Bishara A. A., 2017, J. Phys.: Conf. Ser., 869, 012077
Hathaway D., 2005, 2nd Asia Oceanic Geosciences Society Annual Meeting 2005
Hathaway D. H., 2015, Living Rev. Sol. Phys., 12, 4
Heyvaerts J., Priest E., 1984, A&A , 137, 63
Higginson A. K., Antiochos S. K., DeVore C. R., Wyper P. F., Zurbuchen T. H., 2017, ApJ, 837, 113
Ivanov V. G., Miletsky E. V., 2014, Geomagn. Aeron., 54, 907
Janardhan P., Fujiki K., Ingale M., Bisoi S. K., Rout D., 2018, A&A, 618, A148
Javaraiah J., 2021, Ap&SS, 366, 16
Joshi B., Bhattacharyya R., Pandey K. K., Kushwaha U., Moon Y.-J., 2015, A&A, 582, A4
Kanella C., Gudiksen B. V., 2019, A&A, 621, A95
Klimchuk J. A., 2000, Sol. Phys., 193, 53
Klimchuk J. A., DeForest C. E., 2020, ApJ, 900, 167
Kuckein C., Centeno R., Martínez Pillet V., Casini R., Manso Sainz R., Shimizu T., 2009, A&A, 501, 1113
Lemen J. R. et al., 2012, Sol. Phys., 275, 17
López Fuentes M. C., Klimchuk J. A., Mandrini C. H., 2007, ApJ, 657, 1127
Madjarska M. S., 2019, Living Rev. Sol. Phys., 16, 2
Malanushenko A., Cheung M. C. M., DeForest C. E., Klimchuk J. A., Rempel M., 2022, ApJ, 927, 1
Mikić Z., Lionello R., Mok Y., Linker J. A., Winebarger A. R., 2013, ApJ, 773, 94
Milano L. J., Gómez D. O., Martens P. C. H., 1997, ApJ, 490, 442
Morgan H., Druckmüller M., 2014, Sol. Phys., 289, 2945
Morgan H., Korsós M. B., 2022, ApJ, 933, L27
Moriyasu S., Kudoh T., Yokoyama T., Shibata K., 2004, ApJ, 601, L107
Müller D. et al., 2020, A&A, 642, A1
Nair S., Nayar S., 2008, Indian J. Radio Space Phys., 37, 391
Nakariakov V. M., Kolotkov D. Y., 2020, ARA&A, 58, 441
O'Dwyer B., Del Zanna G., Mason H. E., Weber M. A., Tripathi D., 2010, A&A, 521, A21
Oliver R., Ballester J. L., 1994, Sol. Phys., 152, 481
Pesnell W. D., Thompson B. J., Chamberlin P. C., 2012, Sol. Phys., 275, 3
Poduval B., DeForest C. E., Schmelz J. T., Pathak S., 2013, ApJ, 765, 144
Rappazzo A. F., 2015, ApJ, 815, 8
Reale F., 2014, Living Rev. Sol. Phys., 11, 4
Rochus P. et al., 2020, A&A, 642, A8
SILSO World Data Center, , 2010-2020, International Sunspot Number Monthly Bulletin and online catalogue Royal Observatory of Belgium, avenue Circulaire 3, 1180 Brussels, Belgium The International Sunspot Number World SILSO
Salabert D., García R. A., Pallé P. L., Jiménez-Reyes S. J., 2009, A&A, 504, L1
Seaton D. B. et al., 2021, Nat. Astron., 5, 1029
Sharma A. S., Aschwanden M. J., Crosby N. B., Klimas A. J., Milovanov A. V., Morales L., Sanchez R., Uritsky V., 2016, Space Sci. Rev., 198, 167
The SunPy Community et al., 2020, ApJ, 890, 68
Thompson W. T., 2006, A&A, 449, 791
Uritsky V. M., Klimchuk J. A., 2024, ApJ, 961, 222
van Driel-Gesztelyi L., Green L. M., 2015, Living Rev. Sol. Phys., 12, 1
Watkins N. W., Pruessner G., Chapman S. C., Crosby N. B., Jensen H. J., 2016, Space Sci. Rev., 198, 3
Williams T. et al., 2020a, ApJ, 892, 134
Williams T., Walsh R. W., Peter H., Winebarger A. R., 2020b, ApJ, 902, 90
Williams T., Walsh R. W., Regnier S., Johnston C. D., 2021, Sol. Phys., 296, 102
Xie H., Madjarska M., Li B., Huang Z., Xia L., Wiegelmann T., Fu H., Mou C., 2017, ApJ, 842, 38
Xie J., Shi X., Qu Z., 2018, ApJ, 855, 84
Zhiming S., Xiaoli Y., Zhongquan Q., Hong-Bo L., 2019, MNRAS, 490, 5567

This paper has been typeset from a TEX/LATEX file prepared by the author.